Study of heat transfer and pressure drop for novel configurations of helical tube heat exchanger: a numerical and experimental approach

S. A. Marzouk[1] · M. M. Abou Al-Sood[1] · Emad M. S. El-Said[2] · Magda K. El-Fakharany[1] · M. M. Younes[1]

Abstract

In this study, several unique tube configurations are designed and modeled to examine the thermal and hydraulic performance of a helical tube heat exchanger (HTHE) experimentally and numerically. For cold and hot side tube designs, the numerical investigation is completed using three-dimensional modeling, and the findings are confirmed using experimental data with Reynolds numbers ranging from 16,000 to 25,000. Six configurations named HTHE1, HTHE2, HTHE3, HTHE4, HTHE5, and HTHE6 are tested. The findings showed that as compared to the uniform tube distribution, the new arrangements have a greater overall heat transfer coefficient. The overall heat transfer coefficient has the highest enhancement ratio (125–185%) in the HTHE6 setup with two pathways. Additionally, it is discovered that the pressure drop rises as the Reynolds number increases. The HTHE1 configuration has the highest pressure drop values, whereas configurations with only one pass result in a greater pressure loss when compared to setups with two paths. The values of the coefficient of performance for the HTHE6 are larger than those of other forms, and the coefficient of performance decreases as the Reynolds number increases. The exergy efficiency grows with the rise of Reynolds number where the HTHE6 has the maximum value of exergy efficiency compared to other shapes. The performance of heat transfer is dramatically improved by the novel tube arrangements, although variations in pressure drop and pumping power are only a little affected.

Latin symbols

A_s	Area, m^2
μ	Water viscosity, N s m^{-2}
$\dot{m}$	Water mass flow rate, kg s^{-1}
V	Volumetric flow rate, m^3 s^{-1}
T	Temperature, K
E	Total energy, J
C_p	Specific heat, J kg^{-1} K^{-1}
D_H	Hydraulic diameter, m
g	Gravity, m s^{-2}
P	Corrugation pitch, m
U	Overall heat transfer coefficient, W m^{-2} K^{-1}
ΔP	Pressure drop
v	Water velocity, m s^{-1}
$\dot{Q}$	Heat transfer rate, W
k	Turbulent kinetic energy, J kg^{-1}
G_k	Generation of turbulent kinetic energy, J kg^{-1}
C_ε	Turbulent model constant
C_μ	Turbulent model constant
η	Efficiency

Subscripts

out	Out
in	In
ave	Average
C	Cold
H	Hot
Re	Reynolds number
O	Environment
ex	Exergy

✉ S. A. Marzouk
sef_aleslam@eng.kfs.edu.eg

Emad M. S. El-Said
emspeng@gmail.com

[1] Mechanical Engineering Department, Faculty of Engineering, Kafrelsheikh University, Kafrelsheikh, Egypt

[2] Mechanical Power Engineering Department, Faculty of Engineering, Damietta University, Damietta, Egypt

Abbreviations

COP	Coefficient of performance
HE	Heat exchanger
LPM	Liter per meter
PEC	Performance evaluation criteria
HTHE	Helical tube heat exchanger
HTHE1	Helical tube heat exchanger (1th configuration)
HTHE2	Helical tube heat exchanger (2th configuration)
HTHE3	Helical tube heat exchanger (3th configuration)
HTHE4	Helical tube heat exchanger (4th configuration)
HTHE5	Helical tube heat exchanger (5th configuration)
HTHE6	Helical tube heat exchanger (6th configuration)
LMTD	Logarithmic mean temperature difference
HBD	Heat balance deviation

Introduction

Heat exchangers (HEs) are frequently employed in industry to move heat from one energy source to another, and the effectiveness of the system was directly impacted by its performance. Nuclear reactors, food production, heat recovery, air cooling, chemical processes, and thermal power plants were just a few of the areas where HTHEs were used [1]. When assessing the performance of HEs, variables associated with heat transfer and pressure drop were crucial. Zachár et al. [2] located how to improve heat transfer in HTHEs. Different geometrical characteristics, as well as the influence of the thermal boundary layers on the heat transfer coefficient for both transitional and laminar flow schemes, were investigated using numerical computations. Under varying operating pressure, intake velocity, and pitch, Zhao et al. [3] examined numerically the heat transfer and fluid flow properties of synthesis gas in membrane HTHEs and membrane serpentine tube HEs. Zachár [4] looked at the outer heat transfer in HTHEs caused by natural convection. In the situation of growing temperature disparities between the temperatures of the fluid in the tank and the input of the coil, it was discovered that the outer side heat transfer ratio of any helical tube depended on the inner side flow rate. Genić et al. [5] examined the thermal performance of eight parallel HTHEs. The heat transfer coefficient in the shell side was estimated utilizing the hydraulic diameter-based correlation, according to an analysis of HE thermal performance. Shi and Dong [6] investigated the formation of entropy in a rotating HTHE with laminar convective flow under certain dimensionless parameters, for example, HE performance and heat flux, heat transfer, and frictional drop. With a rising dean number the entropy production from heat transfer over a limited temperature differential reduces. In a HTHE, Mozafari et al. [7] examined the condensation and pressure drop properties of R-600a. The heat transfer rate and pressure drop of the horizontal helical condenser raised by 24–165% and 33–157%, respectively, as compared to the horizontal straight. For these sorts of HEs, the impact of flow, thermodynamic, and geometrical factors on exergetic features were evaluated [8]. The results showed that increasing hot water intake temperature, coil diameter, and hot or cold water flow rates all increase exergy loss. The greatest increase in exergy loss happens in a parallel water flow configuration. Sheikholeslami and Ganji [9] investigated how hydrothermal treatment in water-to-air HEs was affected by perforated and conventional helical fins. According to the results, larger open-area ratios give better thermal performance than lower ones. Zhang et al. [10] used a three-dimensional numerical simulation to explore heat transmission and pressure drop in a helically coiled tube with sphere-shaped corrugations. The results displayed that the secondary streams influenced by centrifugal force had a substantial capability to increase the heat transfer coefficient and that the vortex created by the corrugation construction destroyed the stream boundary layers, increased the flow turbulences intensity, and strengthens the heat transfer process. Omidi et al. [11] looked on the heat transfer applications and turbulent flow properties of twisted double-pipe heat exchangers (DPHE) with four distinct lobed cross sections. The findings revealed that the Nusselt number and pressure drop were increased by a maximum of 240 and 85%, respectively. Zhou et al. [12] looked at how well multi rows HTHEs for surface water source heat pumps transfer heat. With both vertical and horizontal spacing, the inside and outside Nusselt values increased. Mirgolbabaei et al. [13] tested the thermal parameters of vertical HTHEs with variable mass flow rates of shell side, coil to tube radius ratio, and coil pitch. The thermal performances were evaluated with the use of a numerical solution depending on the control-volume method. Javadi et al. [14] evaluated eight different varieties of helical-ground HEs to a single U-tube HE in parameters such as heat exchange coefficient, pressure drop, thermal resistance and performance capabilities, and effectiveness. When compared to other ground HEs, the triple helix HE was shown to have much better thermal performance. Awais et al. [15] employed a CFD technique to study the thermo-hydraulic performance of serpentine tube HEs and Al_2O_3/water-based Nanofluid. The effects of different volumetric water flow rates and serpentine tube cross sections on the heat transfer and pressure drop parameters were investigated. The performance of the heat transfer of the L–H serpentine tubes was found to be superior to that of the other cases. With a small increase in pressure drop, the higher concentrated nanoparticles increased the heat transfer rate. Heydari et al. [16] investigated a shell and helically corrugated coiled tube HE in three dimensions while taking exergy loss into account. For circumstances of low Reynolds numbers, it was shown that employing a helically corrugated coiled tube in the HE rather than a helically plain coiled tube

had greater efficacy. Ali et al. [17] accomplished an experimental and numerical investigation to analyze how shell and coil HEs' geometrical and operational parameters affect the heat transfer. According to the findings, the friction factor tended to decline as the Re number rises, contrary to the Nusselt number. Kumar et al. [18] explored numerically the heat transfer and pressure drop features of micro fin helical coil tubes. With a rise in the fin number and Re number, the Nusselt number (Nu) and pressure drop increased at the same operation status. The Nu was affected by the coil pitches of helical tubes. Miansari et al. [19] used numerical analysis to examine the thermal performance of a HTHE without a fin, with circular fins, and with cut (V-shaped) circular fins applied to the coil at an angle of 15°. Compared to the circular fins, it was discovered that the influence of cut circular fins on the efficacy and heat transfer of helical shell and tube heat exchangers are negligible. Fawaz et al. [20] reviewed studies on HE topology optimization. To increase the effectiveness of topology optimization, three new strategies, including machine learning, model order reduction, and relocating morphable components, were addressed. Aldor et al. [21] demonstrated a unique sine-helical HE with a channel geometry that combined a helical coil and a sine wave shape. In the sine-helical flow, the variation coefficient of the outlet temperature was nearly 100% lower than in the helical channel, indicating higher temperature homogeneity. Wang et al. [22] used response surface analysis to examine the hydraulic and thermal performance of improved construction of HTHE. The improved structure's shell-side performance verification demonstrated that the Performance Evaluation Criterion of optimized tube was 4 to 20% greater than that of helically coiled plain tube. Lei and Bao [23] used helical coiled tubes to conduct an experimental analysis of the heat transfer properties of RP-3 in the phases such as supercritical and liquid. In the helical coiled tube with supercritical laminar mixed convection, correlations were formed. To confirm the association, the investigational data for various fuels, helical radiuses, and tube sizes were employed.

From the previous literature review, it is indicated that many studies investigated the heat transfer and pressure drop for the single HTHE but fewer ones studied the multi-HTHE despite the importance of these configurations such as increasing the surface area of heat transfer. In this study, many novel tube configurations have been designed and modeled in HTHEs to investigate thermal and hydraulic performance experimentally and numerically. Six configurations that have the shape of snakes slithering locomotion named HTHE1, HTHE2, HTHE3, HTHE4, and HTHE6 have been modeled to study the effect of different section lengths of tubes. A numerical investigation has been completed using ANSYS FLUENT, and the results have been confirmed using experimental data with Reynolds numbers ranging from 16,000 to 25,000. The thermal performance

parameters such as U and heat flux have been studied as well as the hydraulic performance parameters like pressure drop and coefficient of performance have been investigated. The streamlines and contours of the temperature, velocity, and pressure distributions will be investigated to understand the fluid flow structure in the HTHE.

Experimental study

Experimental setup

The present experiments are conducted utilizing the experimental test rig introduced in Fig. 1. It consists of a helical tube HE, cold water loop, hot water loop, and signal loop. In the new HE, the hot water flows on the tube side and cold water moves on the shell side. A 500-mm diameter stainless steel shell with 1100 mm in length was used in this study where the core *has* the same length with a 300 mm diameter and the thickness is 2 mm for the shell and the core. Glass wool blanket material is chosen for insulation of the shell external surface with a 33 mm thickness and 0.045 W m^{-1} K^{-1} thermal conductivity. Hot water is pumped by a hot water
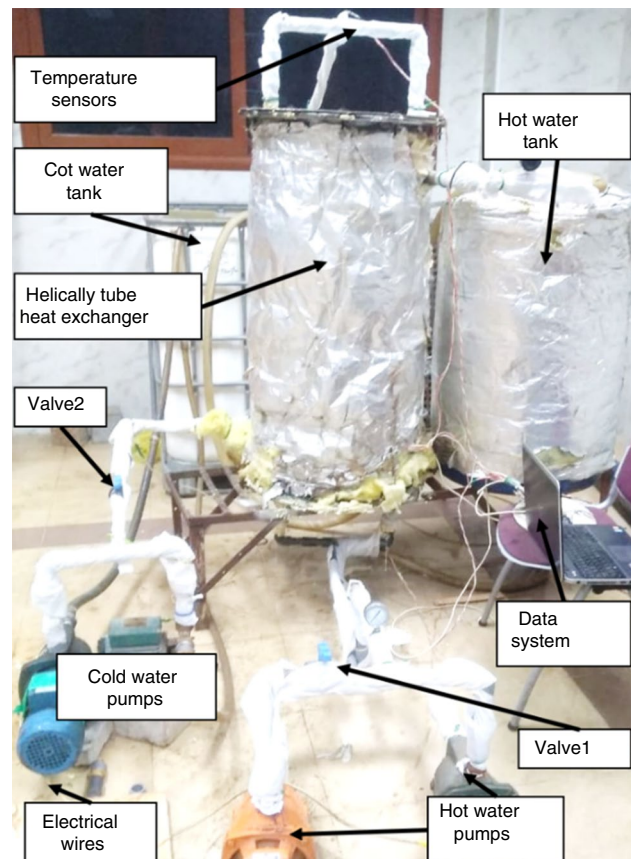

Fig. 1 Photograph of the test rig

pump (HWP) and then is heated up to the desired temperature in the hot water tank by an electric heater (EH) with a 5.3 kW capacity. The hot water moves inside the tube configurations where it is cooled by the cold water in the shell. The hot water volumetric flow rate is adjusted by the valve (V1) shown in Fig. 1. Cold water is cooled by the city water (CW) in the cold water tank where the valve (V2) is used to adjust the cold water flow rate at the required values. Besides, the cold water pump (CWP) is utilized to increase the pressure of the water to move through the shell as seen in Fig. 2.

The data signal system has the temperature, pressure, and flow rates sensors, a data logger (RTC Data Logger Shield), and a personal computer for recording the measured data for all tests (Fig. 2). The sensors (TS1) and (TS2) are used to measure the temperatures of hot water at the tube-side outlet and tube-side inlet, respectively, where the sensors (TS3), and (TS4) are used to indicate the temperatures of cold water at the shell side outlet and shell side inlet, respectively. The magnitude of uncertainty of the temperature sensor is ± 0.44%. The pressure indicators (PS1) and (PS2) were used to record the pressures at the outlet and inlet of the tube side, respectively. The difference between the two values indicates the ΔP across the tube. The error percentage in the pressure sensors is equal to ± 0.38%. The flow meters (FS1) and (FS2) are utilized to indicate the flow rate value in the hot water flow loop and cold flow loop where the precision of flow sensors is ± 0.21%. To increase the quality of time-dependent data recording, every temperature and flow sensor was integrated with an Arduino™ microcontroller. This device has six input channels and is used as a data logger to record all measurements. An open-source software package is used to acquire data from different sensors. Before installation, all the measurement devices were calibrated against standard precision devices to determine the probe's sensibility.

Heat exchanger configurations

Six configurations of the helical tube have been studied. Figure 3 shows three-dimensional models for the six configurations namely HTHE1 which represents one path uniform tube, STHE2 that represents two paths uniform tube, STHE3 is one path high to low configuration, HTHE4 is the two paths high to a low tube shape, STHE5 is one path high to low to high tube configuration, and HTHE6 characterizes two paths high to low to high shape.

Figure 4 shows the dimensions of the basic tube configurations such as uniform, low to high, high to low to high, and low to high to low that were used to construct the six tube configurations. The first and second configurations (HTHE1, HTHE2) consist of four uniform basic tubes, and the configurations HTHE3 and HTHE4 consist of two low to high shapes with the same overturned shape. The HTHE5 and HTHE6 configurations involve two low to high to low and high to low to high shapes connected.

The photograph of the basic copper tube configurations used in this study is presented in Fig. 5. Those configurations are designed to have the same surface area, and their dimensions are determined according to this situation. The fabrication process begins with shaping the tube by a bending tool according to the tube diameter as seen in Fig. 5(a–d). The drilling process at the inlet and outlet of hot water is performed and manifold tubes are welded and the full configuration is inserted between the shell and the core as seen in Fig. 5(g). More details about the parameters and dimensions of tubes are investigated in Table 1.

Data reduction

The heat transfer from the hot water to the cold water in the HE could be determined by:
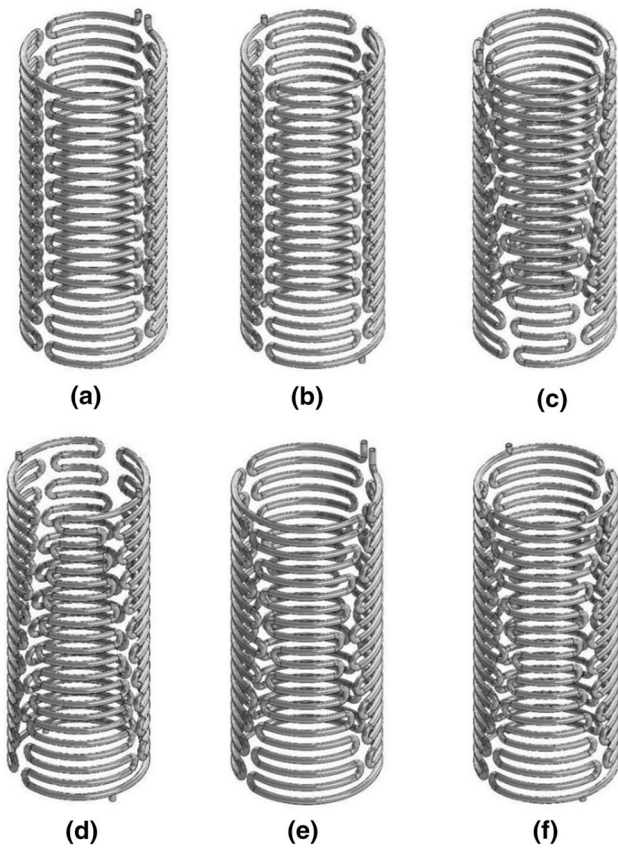
Fig. 2 Test rig layout
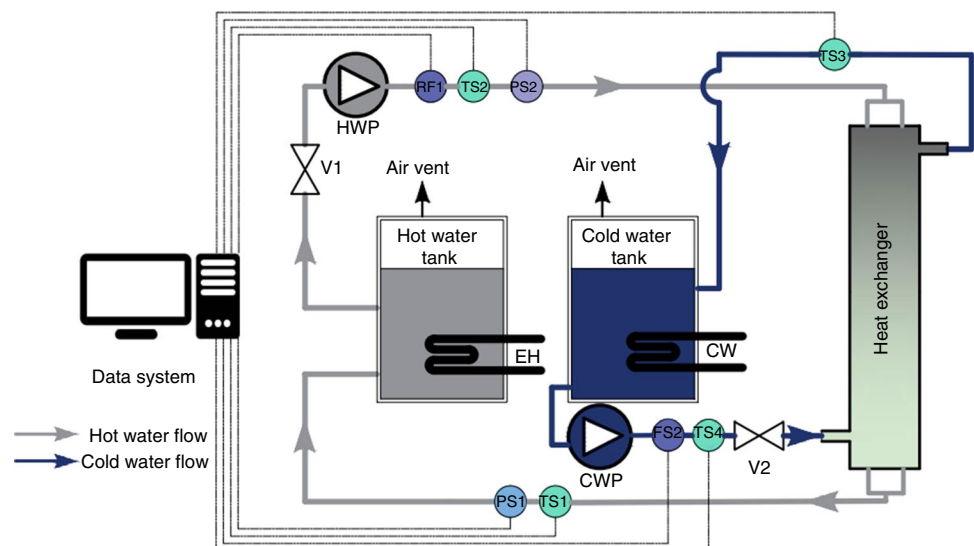
Fig. 3 Three-dimensional model for six configurations of the helical tube **a** HTHE1, **b** HTHE2, **c** HTHE3, **d** HTHE4, **e** HTHE5, **f** HTHE6
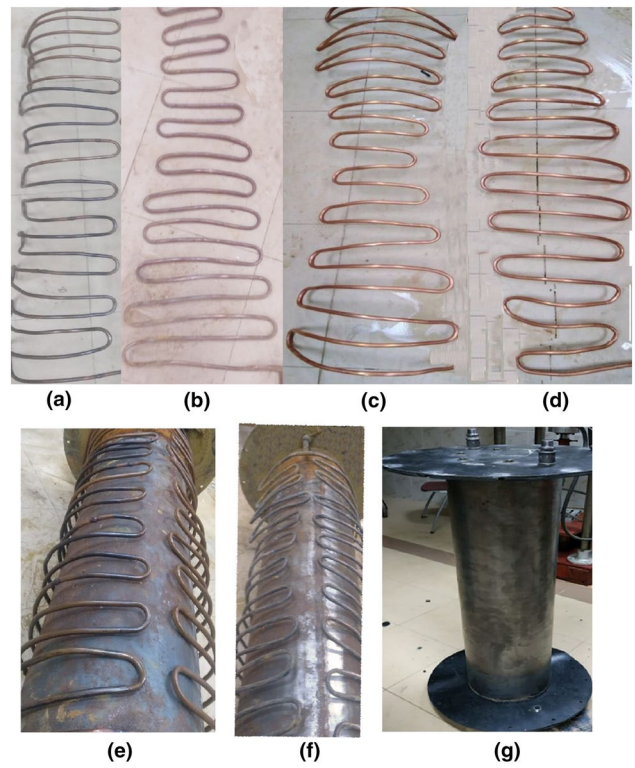

Fig. 5 Photographs of basic tube configurations before bending process **a** uniform, **b** low to high, **c** high to low to high, and **d** low to high to low, tube configurations **e** HTHE2, **f** HTHE4, and **g** shell and core

Fig. 4 Dimensions in millimeters of basic tube configurations **a** uniform, **b** low to high, **c** high to low to high, **d** low to high to low
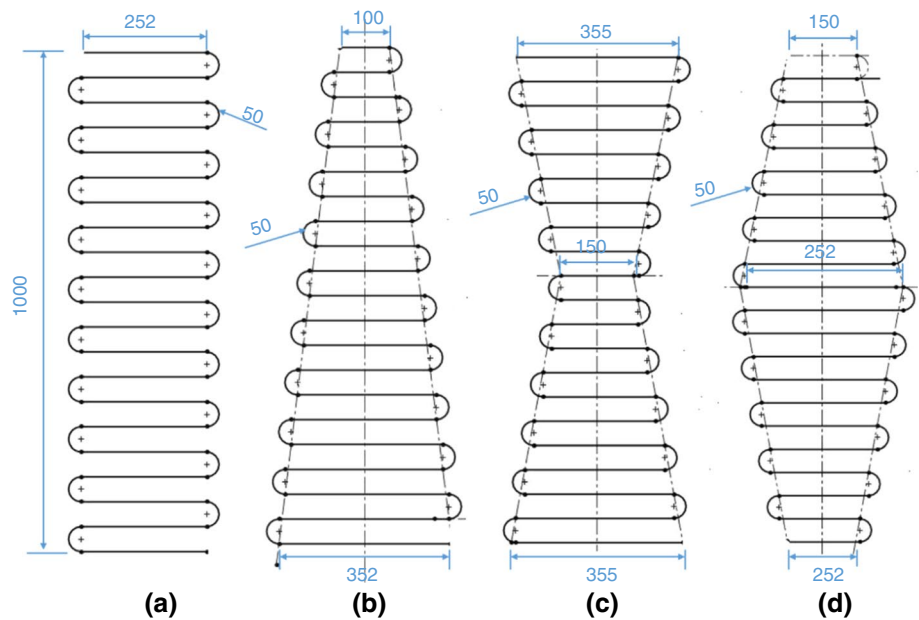
Table 1 Parameters and dimensions of tubes

Parameter	Value
Material	Copper
Inner diameter	13.41 mm
Outer diameter	15.87 mm
Helical diameter	400 mm
Thickness	1.23 mm
Height	1000 mm
Pitch	50 mm

$$\dot{Q}_H = \dot{m}c_{p,H}\left(T_{H,in} - T_{H,out}\right) \tag{1}$$

The heat quantity of the cold water in the HE can be calculated by:

$$\dot{Q}_C m_C c_{p,C} T_{C,out} - T_{C,in} \tag{2}$$

So that the average heat quantity could be calculated based on the heat transfer quantity of the cold and hot sides.

$$\dot{Q}_{ave} = \frac{\dot{Q}_C + \dot{Q}_H}{2} \tag{3}$$

The overall heat transfer coefficient (U) can be calculated by [24]:

$$U = \frac{\dot{Q}_{Ave}}{A_s F \Delta T_{LMTD}} \tag{4}$$

where A_s is the surface area of the helical tubes configurations, F is the correlation factor of the logarithmic mean temperature difference that is determined by the heat exchanger's geometry and the temperatures at the hot and cold water streams' input and output, and it is a constant with a value of 0.96 [24], and ΔT_{LMTD} is the logarithmic mean temperature difference that can be determined by:

$$\Delta T_{LMTD} = T_{H}, \text{in} - T_{C,out} - T_{H}, \text{out} \\ - T_{C,in} \ln T_{H,in} - T_{C,out} T_{H,out} - T_{C,in} \tag{5}$$

The efficiency of the helical tube configurations is estimated by the coefficient of performance (COP) defined by [25]:

$$COP = \frac{\dot{Q}_{Ave}}{V \Delta P} \tag{6}$$

where V is the volumetric flow rate and ΔP is the pressure difference between the outlet and inlet of the hot water side. The Re at the inlet of the tube side can be calculated by:

$$Re = \frac{\rho v D_H}{\mu} \tag{7}$$

The hot water velocity and density are defined by v and ρ, respectively. D_H is the hydraulic diameter and it equals the diameter of the entrance tube at the inlet of the hot water and μ is water viscosity. The exergy efficiency can be calculated by this equation [26]:

$$\eta_{ex} = 1 - \left\{ \frac{T_o\left[\dot{m}_H c_{p,H} \ln\left(\frac{T_{H,out}}{T_{H,in}}\right) + \dot{m}_C c_{p,C} \ln\left(\frac{T_{C,out}}{T_{C,in}}\right)\right]}{\dot{m}_H c_{p,H}\left[\left(T_{H,out} - T_{H,in}\right) - T_o \ln\left(\frac{T_{H,out}}{T_{H,in}}\right)\right]} \right\} \tag{8}$$

The exergy efficiency can be expressed in η_{ex} where To is the surrounding environmental temperature and its value is about 23.5 °C in this study. The heat flux can be calculated by the following equation depending on the average heat quantity and surface area of the tube:

$$\dot{q} = \frac{\dot{Q}_{ave}}{A_s} \tag{9}$$

Heat balance deviation

One of the most critical aspects in determining how well an experiment will perform is the heat balance deviation (HBD). The following equation is used to compute the HBD depending on Eqs. (1, 2 and 3) [27].

$$HBD = \frac{\dot{Q}_H - \dot{Q}_C}{\dot{Q}_{ave}} \tag{10}$$

The HBD must be smaller than 5.0%, and the current study's results indicate that this principle was satisfied.

Experimental uncertainty analysis

The approach outlined by Holman [28] is used in the present study to compute the greatest uncertainty in the investigational data. By evaluating derivatives of the necessary variable concerning each experimental quantity and including unknown uncertainties, the analysis of experimental quantities that contribute to system uncertainty was presented. The investigative uncertainty for an experimental variable (WR) is computed in experiments by:

$$W_R = \sqrt{\sum_{i=1}^{n}\left(\frac{\partial R}{\partial X_i} \cdot W_i\right)^2} \tag{11}$$

So, each result is quantified as:

$$R_i = R\left(X_1, X_2, \ldots, X_n\right) \tag{12}$$

Table 2 Maximum uncertainty magnitudes for different parameters

| Parameter	Value %
Water mass flow rate	±0.19
Temperatures	±0.32
Overall heat transfer coefficient	±3.881
Coefficient of performance	±5.23
Exergy efficiency	±5.71
Pressure drop	±0.81

where uncertainty of the experimental outcomes is presented by $W_R, X_1, X_2, \ldots, X_n$ indicating independent variables, and $W_1, W_2, \ldots, W_n$ explaining uncertainty in the subsequent variables. The uncertainties determined in the analysis are computed and summarized in Table 2.

Numerical study

In this section, a description of the numerical model used in simulation, mesh generation, governing equation that controls the process of heat transfer and mass continuity, model validation according to the experimental setup, and numerical results represented in temperature and velocity contours were presented.

Physical model

Figure 6 presents the representational diagram of the arrangement of tubes inside the shell of the HE with cold
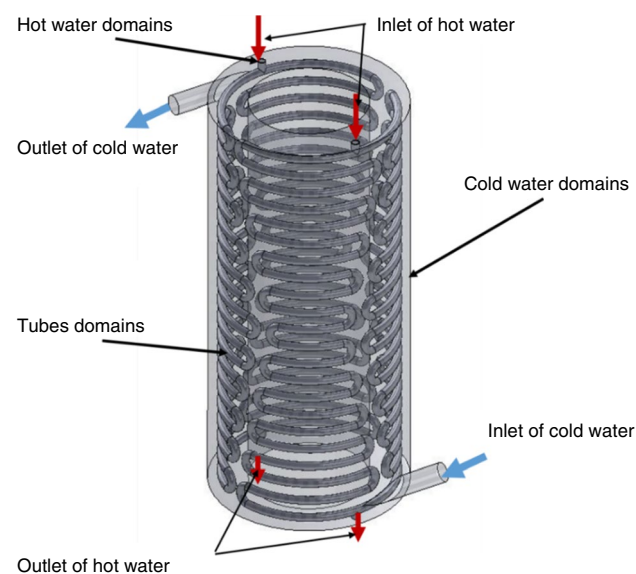
Fig. 6 Model for domains of cold water, hot water, and tubes
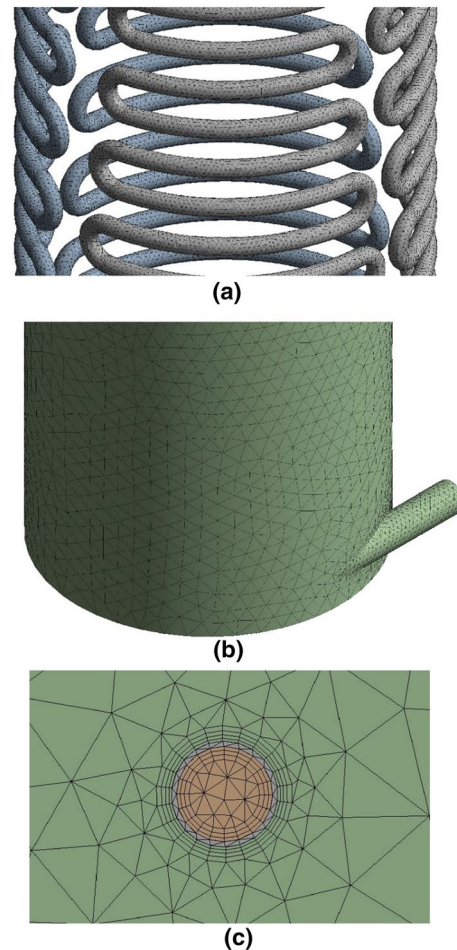
Fig. 7 Mesh generation for **a** copper tube, **b** inlet of the cold water, **c** inflation layers at tube walls

water and hot water domains. A stainless steel shell of 1100 mm in length with a 500 mm diameter was used, whereas the core has the same length with a 300 mm diameter.

Mesh generation

Complex systems consisting of physical domains of the tube bundle, hot water, and cold water domains have meshed with an unstructured mesh of type tetrahedron. Mesh refinements were applied for the zones beside tube configurations. Figure 7 shows the mesh grid for the tubes, the cold water domain, and inflation layers at the cold and hot sides walls. Five grid systems with 1.61, 1.721, 1.982, 2.021, and 2.13 million elements are produced to satisfy the mesh independence check as seen in Fig. 8. The error in outlet hot water temperature values between the third and fourth grid number system is about 0.35%. So, the model that contains 2.021 million cells is used for this investigation.
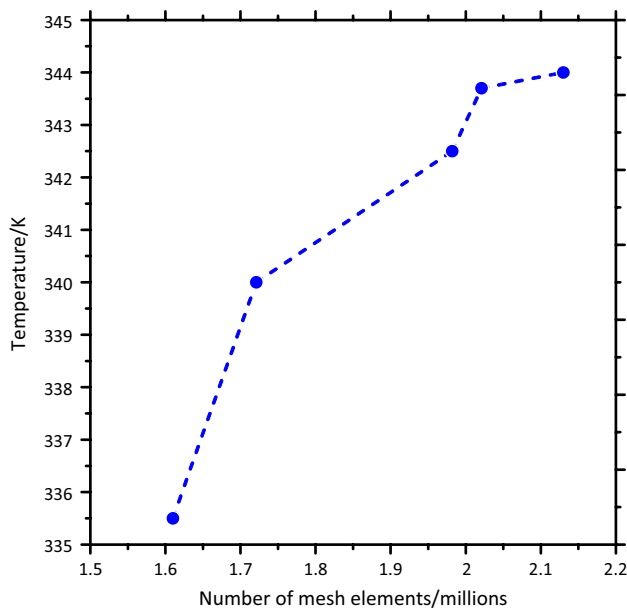
Fig. 8 The relation between the outlet temperature of hot water and the number of grid elements

CFD procedure and boundary conditions

The numerical study is completed using Ansys Fluent for cold and hot side, tube configurations. The 3-D model was performed with Solidworks and then transmitted into Fluent with double precision, and a pressure-based solver is chosen to explain the steady-state situation. The realizable k-ε model is indicated as the turbulent model as stated by the previous studies of various turbulence models for HEs with standard wall functions treatment [18, 29]. As the helical HEs configurations are in the vertical position, the effect of gravity is specified in the modeling of the HE. The inlets of the shell and tubes are established with mass flow inlets and the outlets of those are set as pressure outlets to determine the pressure drop that occurred in

the tube according to boundary conditions. The tube-side mass flow rates of hot water range from 0.22 to 0.35 kg s⁻¹, whereas the cold water mass flow rate is constant at 0.35 kg s⁻¹. It is indicated that the realizable k-ε turbulence model is more operational and accurate on high *Re* conditions [30]. Some assumptions are utilized to simplify the simulation such as incompressible fluids, steady fluid flow, constantly solid and fluid properties, and no-slip walls. More information about boundary and initial conditions and solution methods is presented in Table 3.

Governing equation

The governing equations for continuity, momentum, and energy in the CFD modeling are illustrated in the three equations [15]. The continuity equation of water flow can be defined by:

$$\frac{\partial}{\partial x_i}\left(\rho u_i\right) = 0 \tag{13}$$

where ρ and u_{nit} characterize the density and velocity of water fluid, respectively. The momentum equation can be expressed as:

$$\frac{\partial}{\partial x_i}\left(\rho u_i u_j\right) = -\frac{\partial P}{\partial x_J} + \frac{\partial}{\partial x_J}\left[\mu\left[\frac{\partial u_i}{\partial x_J} + \frac{\partial u_j}{\partial x_i} - \frac{2}{3}\delta_{ij} + \frac{\partial u_i}{\partial x_J}\right]\right] + \frac{\partial}{\partial x_i}\left(-\rho u_i u_j\right) \tag{14}$$

where μ, u_i, u_j, u_i and u_j represent water viscosity, fluid velocity in *x* and *y* directions, and fluctuated water velocity in *x* and *y* directions, respectively. $\rho u_i u_j$ represent turbulent shear stress where the energy equation can be indicated as:

$$\frac{\partial}{\partial x_i}\left[u_i(\rho E + P)\right] = \frac{\partial}{\partial x_i}\left[k_{eff}\left(\partial T/\partial x_i\right)\right] \tag{15}$$

Table 3 Boundary and initial conditions and solution methods

Boundary conditions		
Location	Flow conditions	Thermal conditions
Inlet of hot water	Mass flow inlet (0.22–0.35) kg s⁻¹	Temperature (363 K)
Inlet of cold water	Mass flow inlet (0.35 kg s⁻¹)	Temperature (363 K)
Outlet of hot water	Pressure outlet (Atmospheric pressure)	Temperature (363 K)
Outlet of cold water	Pressure outlet (Atmospheric pressure)	Temperature (363 K)
Outer surfaces	Stationary wall (no slip)	Heat flux (0.0 W m⁻²)
Methods		
Pressure velocity scheme	Simple	
Special discretization for momentum	Second order upwind	
Special discretization for energy	Second order upwind	
Special discretization for pressure	Second order	

While ρ is the water density, E represents overall energy, T explains the temperature and k_{eff} is effective thermal conductivity.

Turbulence model

Due to its excellent trade-off between computing effort and accuracy, two-equation turbulence models are particularly popular. The zero equation models cannot compare to the sophistication of the two-equation models. Separate transport equations are used to determine the velocity and length scale. The two-equation turbulence model with the most widespread use is the k-model. The majority of general-purpose CFD programs have used this renowned turbulence model. It has a well-proven regime of predictive capacity and is stable, numerically robust, and reliable. For a wide range of engineering interest flows, this model offers accurate forecasts. K is the kinetic energy of turbulence, which is determined as the velocity fluctuations variance. To adjacent the scheme of RANS equations, a turbulence model could be essential. Check on previous researches [29, 31, 32], a realizable k-ε model, as well as a standard wall function, are accomplished that determine the equations for the turbulent kinetic energy and the dissipation as accessible [33, 34]:

$$\frac{\partial}{\partial t}(\rho k) + \frac{\partial}{\partial x_i}\left(\rho k u_i\right) = \frac{\partial p}{\partial x_j}\left(\alpha_k \mu_{\text{eff}} \frac{\partial k}{\partial x_j}\right) - \rho \varepsilon + G_k \qquad (16)$$

$$\frac{\partial}{\partial t}(\rho \varepsilon) + \frac{\partial}{\partial x_i}\left(\rho \varepsilon u_i\right) = \frac{\partial}{\partial x_j}\left(\alpha_\varepsilon \mu_{\text{eff}} \frac{\partial k}{\partial x_j}\right) + C_{1\varepsilon}^* \frac{\varepsilon}{k} G_K - C_{2\varepsilon}\rho \frac{\varepsilon^2}{k} \qquad (17)$$

In the above equation, $= \left(2E_{ij} \cdot E_{ij}\right)^5 \frac{K}{\varepsilon}$, $C_{1\varepsilon}^* = C_{1\varepsilon} - \frac{\eta\left(1 - \eta/\eta_0\right)}{1 + \beta\eta^3}$ and $\mu_{\text{eff}} = \mu + \mu_t$ where $\mu_t = \rho c_\mu \frac{k^2}{\varepsilon}$. E_{ij} and G_k are defined as:

$$E_{ij} = \frac{1}{2}\left(\frac{\partial u_i}{\partial x_j} + \frac{\partial u_j}{\partial x_i}\right) \qquad (18)$$

$$G_k = \mu_t\left(\frac{\partial u_i}{\partial x_j} + \frac{\partial u_j}{\partial x_i}\right)\frac{\partial u_i}{\partial x_j} \qquad (19)$$

The empirical constants for the RNG k-ε model are $C_\mu = 0.0845$, $C_{1\varepsilon}^* = 1.42$, $C_{2\varepsilon}^* = 1.68$, $\beta = .012$ [35].

Model verification

Comparing the numerical and experimental outcomes was achieved for confirming the accuracy depending on the physical model. Figure 9 displays the comparison between the U for the experimental and numerical results for HTHE1,
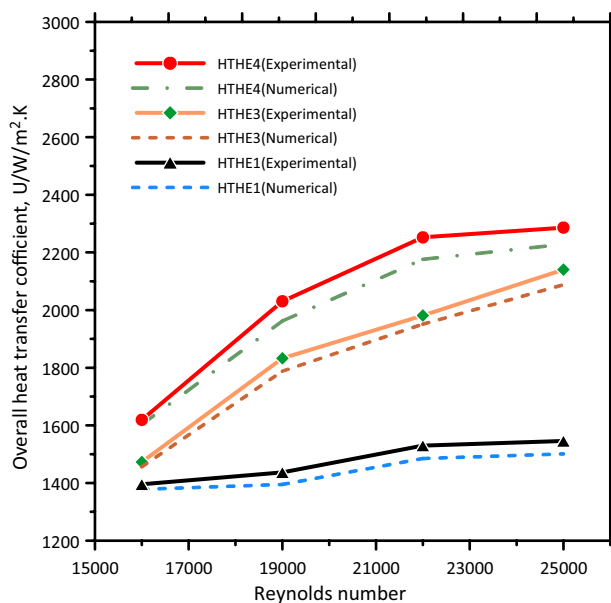
Fig. 9 The U for the experimental and numerical results for HTHE1, HTHE3, and HTHE4 configurations

HTHE3, and HTHE4 configurations versus the Re. The numerical results indicated similar performances in the same case of experimental ones. The regular differences between numerical and experimental results for the U are around 2.93%, 2.47%, and 3.18% for HTHE1, HTHE3, and HTHE4, respectively. In general, the difference is acceptable for simulation errors and these errors for modeling are effective and accurate in this study.

Results and discussion

The relation between the overall heat transfer coefficient (U) and Re for the six configurations such as HTHE1, HTHE2, HTHE3, HTHE4, HTHE5, and HTHE6 are investigated in Fig. 10 for Re range from 16,000 to 25,000. It is indicated that the U increases with the rise of the Re for all configurations. It is detected that the novel configurations have higher values of U compared to the uniform tube distribution (HTHE1). The HTHE6 consists of low to high to low and high to low to high tube shapes with two paths, and it is similar to a snake motion outline, achieving the maximum U compared to the other configurations. it can be indicated that the snake motion outline for one or two paths has the maximum enhancement of heat transfer. This may be due to the increase in the turbulence level inside the tubes as a result of this kind of motion. At the same Re, the uniform tube often produces a lower heat transfer coefficient than other serpentine tubes. The significant impact of different geometrical perimeters on thermal performance may be described by
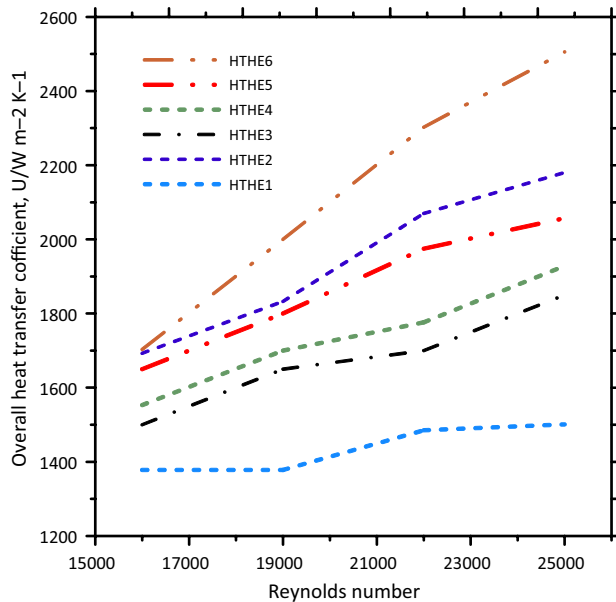
Fig. 10 The relation between the U and Re for the six configurations

Fig. 11 The relation between the U ratio and Re for the six configurations

the secondary flows that occur when a flowing fluid passes through an indirect helical tube. This rotating flow thus tends to increase the rate at which hot and cold fluids mix in the boundary layer, providing a larger convective heat transfer rate. Variations in geometrical forms have a big impact on secondary flows.

The U ratio is the overall heat transfer coefficient of tube configuration divided by the U of HTHE1(U/U_{HTHE1}). Figure 11 shows the U ratio versus the Re for the configurations like HTHE2, HTHE3, HTHE4, HTHE5, and HTHE6 based on the only path uniform tube shape. It is indicated that the heat transfer coefficient ratio of the two path configurations is higher than those of one path configuration. The enhancement ratio of the U for HTHE2, HTHE3, HTHE4, HTHE5, and HTHE6 configurations are ranging between 124–142%, 118–128%, 115–150%, 130–164%, and 125–185%, respectively, compared with HTHE1. The HTHE6 configuration with two paths has the maximum enhancement ratio for U (125–185%).

The pressure drops versus the Re for the six configurations such as HTHE1, HTHE2, HTHE3, HTHE4, HTHE5, and HTHE6 is illustrated in Fig. 12. It is indicated that the pressure drop for all configurations increases with the growth of Re where the HTHE1 configuration has the maximum values of pressure drop. It is observed that the configurations that have one pass lead to more pressure drop compared to the two path configurations. The difference in geometric section lengths does not seem to have an obvious influence on pressure drop where the percentage of pressure drop between the configurations HTHE1, HTHE3, and
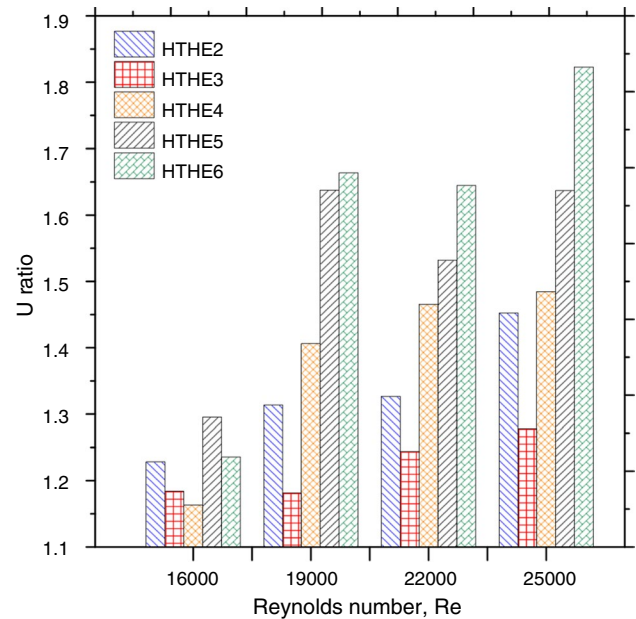
HTHE5 is very small, and the difference between pressure drop for HTHE2, HTHE4, and HTHE6 is almost slight. This is an indication that different tube configurations lead to an important role in developing greater heat transfer performance at the expenditure of insignificant pressure drop.
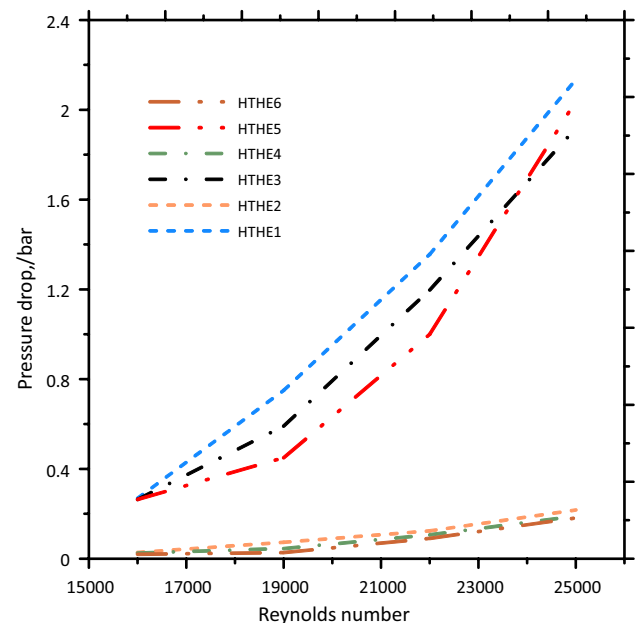

Fig. 12 The pressure drop in the tube side versus the Re for the six configurations **a** HTHE1, **b** HTHE2, **c** HTHE3, **d** HTHE4, **e** HTHE5, **f** HTHE6

The pressure drop ratio is the pressure drop of tube configurations divided by the pressure drop of HTHE1. The relation between the pressure drop ratio and Re number for HTHE2, HTHE3, HTHE4, HTHE5, and HTHE6 is illustrated in Fig. 13. It is indicated that the pressure drop ratio for tube configurations HTHE3 and HTHE5 is near 100% and that can be explained as those configurations have one pass. The configurations HTHE2, HTHE4, and HTHE6 have approximate values of pressure ratio where they have two passes, and those values are very small compared to one path configurations. Depending on the energy equation [36], the parallel tubes have the same pressure drop whereas the pressure losses depend on the length of the tubes and the square of the volumetric flow. In the two-path configurations, the branch length and the volumetric flow are reduced to the half values of the single path so that there is a large difference between the two and one-path tube configurations. It is observed that this big difference does not appear with U because it depends on the surface area and inlet and outlet temperatures.

The relation between the coefficient of performance (COP) and the *Re* for the six configurations is illustrated in Fig. 14 where the values of COP decrease with the growth of the *Re* number. It specified that the values of COP for the HTHE6 are higher than those of other shapes at the same range of Re number. The ratio of COP for the new configurations to uniform helical tube HE is always greater than one which means that HTHE6 is superior to the helical tube HE. The enhancement ratio of COP for HTHE is about 7.6.
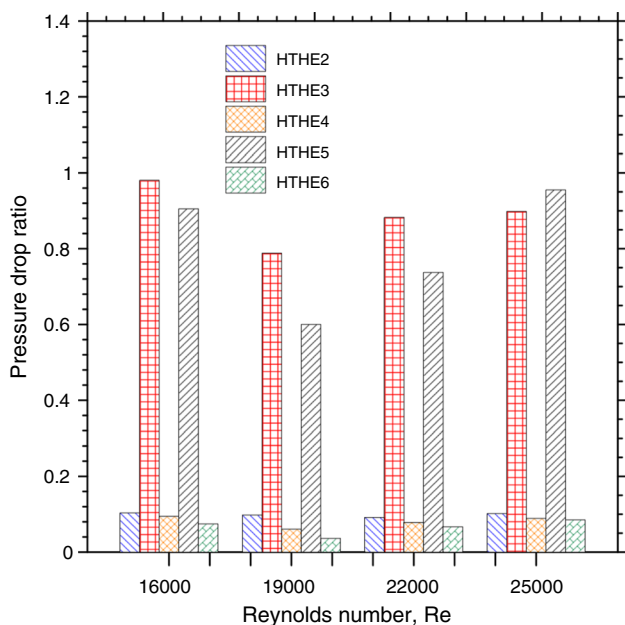

Fig. 14 COP versus the Re for the six configurations **a** HTHE1, **b** HTHE2, **c** HTHE3, **d** HTHE4, **e** HTHE5, **f** HTHE6

The pressure COP ratio is the COP of configurations HTHE2, HTHE3, HTHE4, HTHE5, and HTHE6 divided by the COP of HTHE1shape. The relation between COP ratio and Re for the tube configurations is investigated in Fig. 15. The HTHE6 has the maximum enhancement of COP ratio achieving the values 110 to 126% compared to other
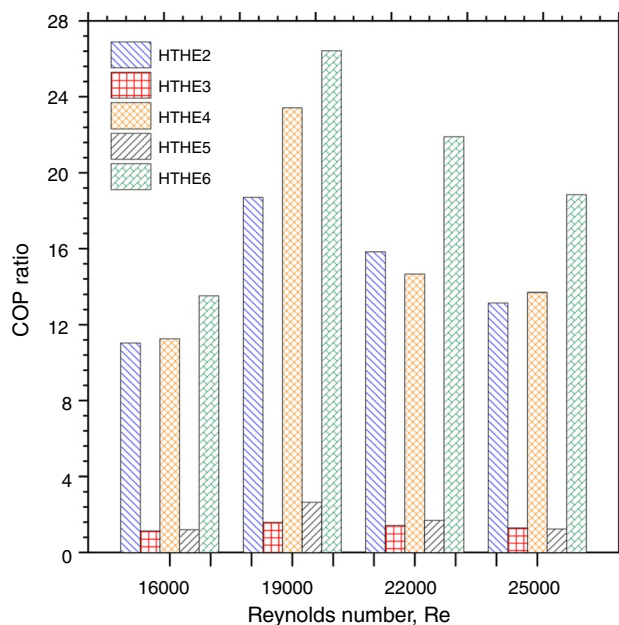

Fig. 13 The relation between the pressure drop ratio and Re for HTHE2, HTHE3, HTHE4, HTHE5, and HTHE6

Fig. 15 The relation between COP ratio and Re for HTHE2, HTHE3, HTHE4, HTHE5, HTHE6

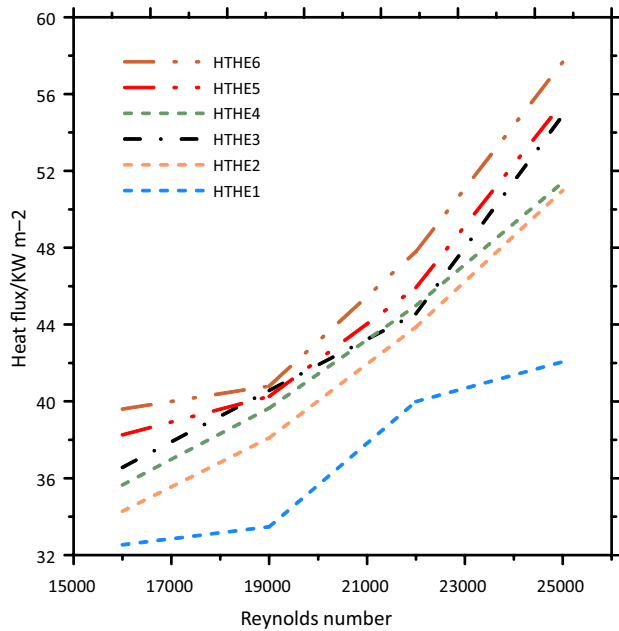**Fig. 16** Heat flux versus Re for the six configurations **a** HTHE1, **b** HTHE2, **c** HTHE3, **d** HTHE4, **e** HTHE5, **f** HTHE6
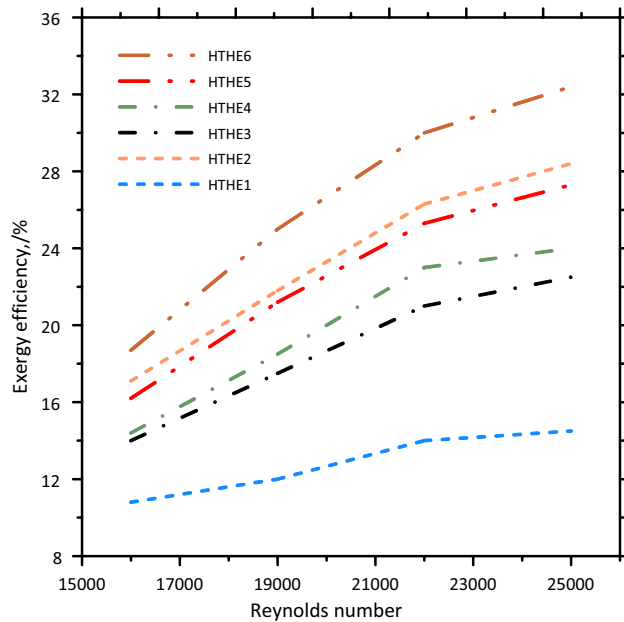

Fig. 18 Temperature distributions for the configurations **a** HTHE1, **b** HTHE2, **c** HTHE3, **d** HTHE4, **e** HTHE5, **f** HTHE6

Fig. 17 Exergy efficiency versus Re for the six configurations **a** HTHE1, **b** HTHE2, **c** HTHE3, **d** HTHE4, **e** HTHE5, **f** HTHE6
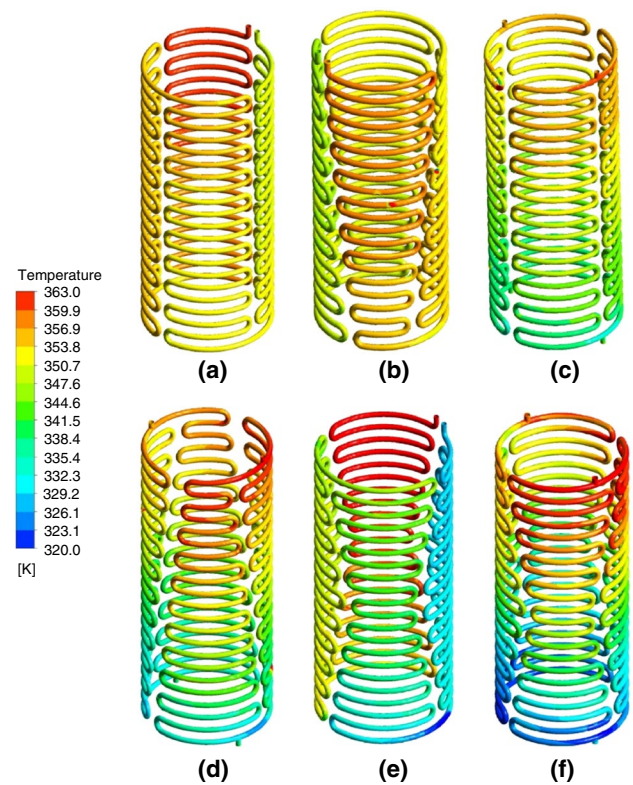
configurations. It is observed that the COP ratio of HTHE2, HTHE4, and HTHE6 that contain two tube paths is higher than those of configurations that consist of one path that can be explained because the COP is reverse proportional to pressure drop and.

The relation between heat flux versus *Re* for the six configurations such as HTHE1, HTHE2, HTHE3, HTHE4, HTHE5, and HTHE6 can be observed in Fig. 16. The heat flux steadily improved from 38,000 to 58,000 (w/m^2) for the HTHE6 configuration, whereas the heat flux values are observed between 32,100 and 42,000 (w/m^2) for the HTHE1 shape.

The relation between exergy efficiency versus Re for the six configurations such as HTHE1, HTHE2, HTHE3, HTHE4, HTHE5, and HTHE6 is investigated in Fig. 17. The exergy efficiency steadily increases with the rise of Reynolds number where the HTHE6 has the maximum value of exergy efficiency compared to other shapes. That can be explained as the HTHE6 shape achieves the maximum heat transfer,
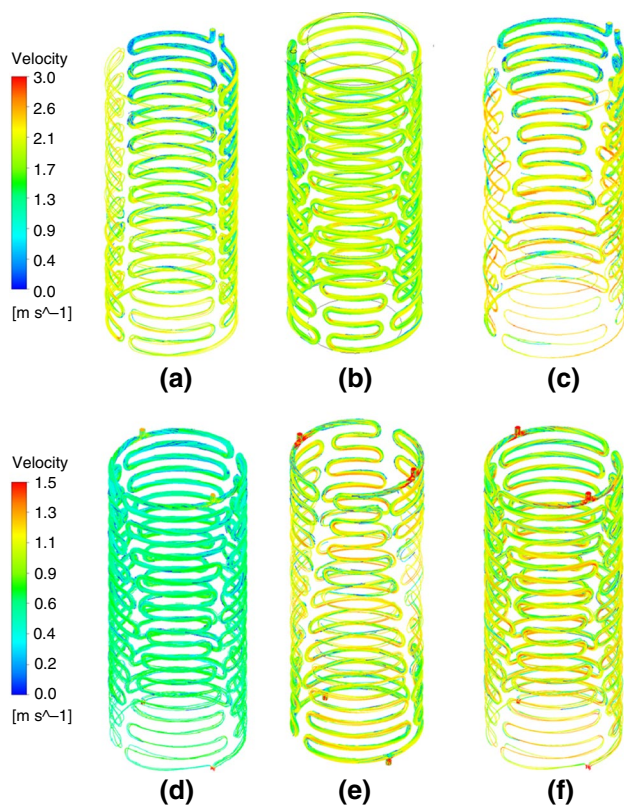
Fig. 19 The velocity distribution of hot water for the six tube configurations **a** HTHE1, **b** HTHE2, **c** HTHE3, **d** HTHE4, **e** HTHE5, **f** HTHE6
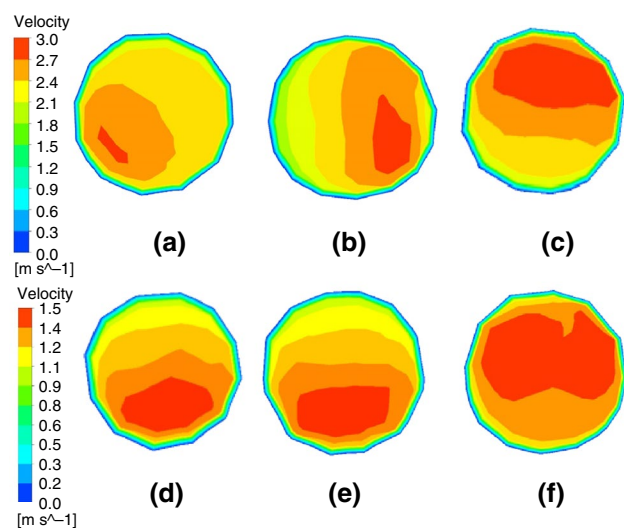

Fig. 20 The contours of the velocity at the cross section of the six tube configurations **a** HTHE1, **b** HTHE2, **c** HTHE3, **d** HTHE4, **e** HTHE5, **f** HTHE6

the hot water temperature drops increase so that the exergy losses decrease, and the exergy efficiency enhances.

The 3-D model was performed and verified with the experimental results and the error percentage between the numerical and the experimental findings are acceptable and then the numerical results have been extracted in contours and streamlines of temperature, velocity, and pressure. Temperature distributions of tube surfaces for the studied configurations (HTHE1, HTHE2, HTHE3, HTHE4, HTHE5, and HTHE6) are investigated in Fig. 18. This can be explained as more heat transfers from the hot-water side to the cold-water side in the HTHE6 comparing to the other configurations.

Figure 19 illustrates the pathlines of velocity distributions of hot water for the six tube configurations, verifying the considerable effects of the new type on the fluid flow. Variations in geometric configurations can have significant implications on thermal performance, which may be described by the fact that when a flowing fluid flows across secondary networks, additional flow influences are at work. This rotating flow tends to increase the mixing rate of hot and cold water fluids in the boundary layer, leading to a larger convective heat transfer rate. The impact of new arrangements on secondary flows is significant as seen in Fig. 20. At the upstream end of low to high tubes, a short straight section induces intense dean vortices, and a detectable temperature gradient can be obtained. The high to low to high tube's entrance and departure should produce an effect comparable to that of the tube's center.

The hot water pressure distribution for the six helical tubes HE configurations is investigated in Fig. 21. The effect of one pass and tube passes configuration is observed where the two passes show less pressure drop compared to the only one pass tube configurations. This suggests that novel tube configurations are crucial in accomplishing superior heat transfer performance at a negligible pressure drop. The impact of a few cutting-edge tube designs on the HTHE's thermal and hydraulic efficiency. The discussion demonstrated how the various layouts considerably changed the efficiency of heat transfer while only slightly altering variations in pressure drop and, thus, pumping power. The pressure loss is independent of the volumetric flow and tube length, whereas the pressure loss is constant for parallel tubes. There is a significant difference between the two and one-path tube designs because in the two-path configurations, the branch length and volumetric flow are decreased to the half values of the single path.
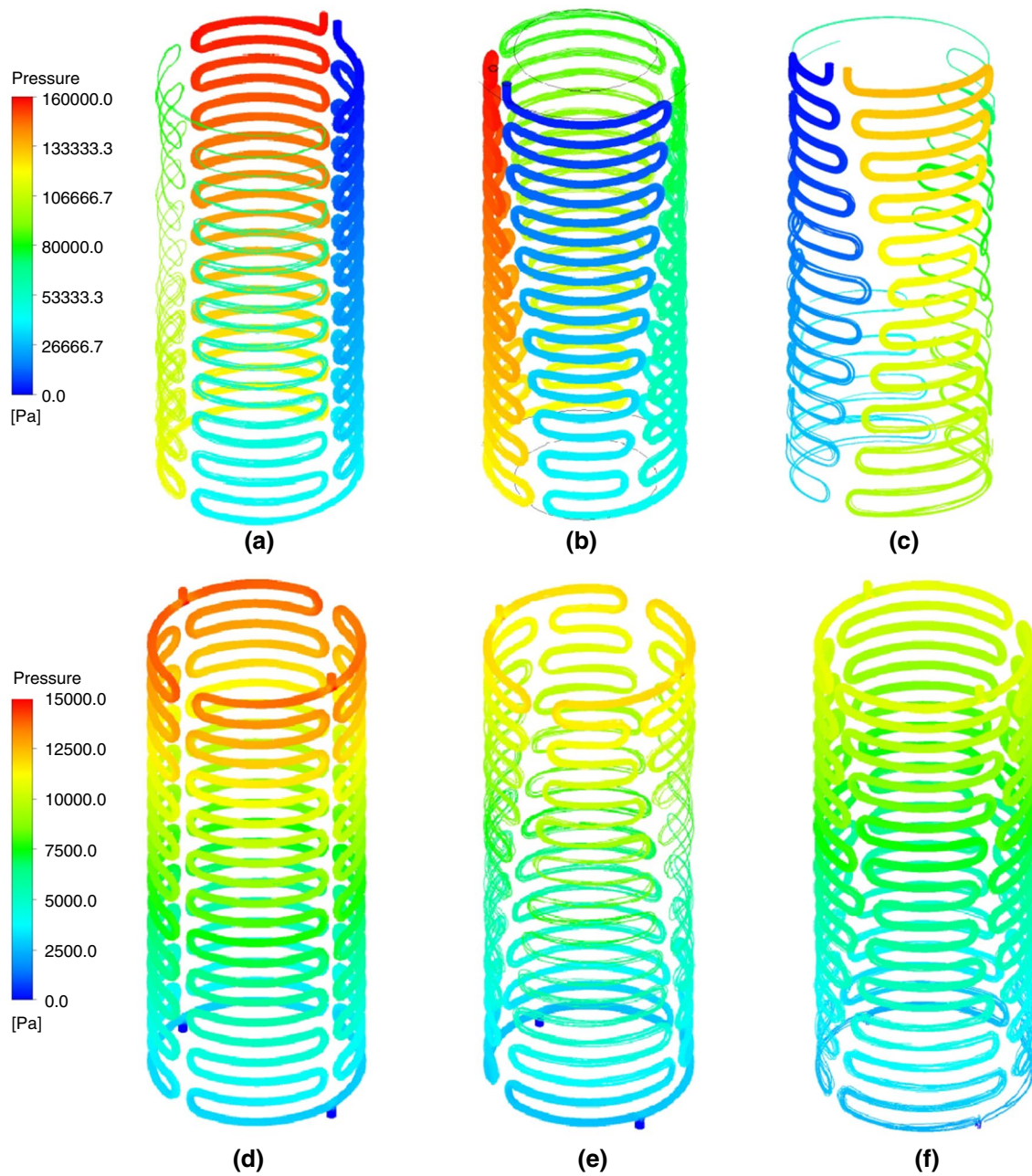
Fig. 21 The pressure distribution of hot water for the six tube configurations **a** HTHE1, **b** HTHE2, **c** HTHE3, **d** HTHE4, **e** HTHE5, **f** HTHE6

Conclusions

In this paper, many novel tube configurations have been designed and modeled in *HTHE*s to investigate their thermal and hydraulic performance. The numerical study is completed using ANSYS FLUENT for cold side, hot side, and tube configurations. The numerical outcomes are validated with the experimental results with Reynolds numbers ranging from 16,000 to 25,000. Six configurations namely HTHE1, HTHE2, HTHE3, HTHE4, HTHE5, and HTHE6 are studied. The main conclusions can be mentioned in those points:

- The novel configurations such as HTHE2, HTHE3, HTHE4, HTHE5, and HTHE6 have higher overall heat transfer coefficient (U) compared to the uniform tube distribution (HTHE1).
- The enhancement ratio of U for HTHE2, HTHE3, HTHE4, HTHE5, and HTHE6 configurations are (124%-142%), (118%-128%), (115%-150%), (130%-164%), and (125%-185%).

- The HTHE6 configuration with two paths has the maximum enhancement ratio for *U* (125%-185%).
- The pressure drops increases with the rise of the Reynolds number. The HTHE1 configuration has the maximum values of pressure drop where the configurations that have one pass lead to more pressure drop compared to the two path configurations.
- The COP decreases with the rise of the *Re* where the values of COP for the HTHE6 are higher than those of other shapes.
- The heat flux gradually enhanced from 38000 to 58000 (W m^{-2}) for the HTHE6 configuration, while the heat flux value is observed between 32100 and 42000 (W m^{-2}) for the HTHE1 configuration.
- The exergy efficiency grows with the rise of Reynolds number where the HTHE6 has the maximum value of exergy efficiency compared to other shapes.
- Different tube configurations significantly altered heat transfer performance, and the effects of one pass and tube pass configuration are observed.
- The contours and streamlines for the velocity, temperature, and pressure distribution of hot water introduce more crucial explanations for heat transfer in tubes.

Declarations

Conflict of interest The authors state that none of their known personal or financial conflicts could have affected the research reported in this study.

References

1. Naphon P. Thermal performance and pressure drop of the helical-coil heat exchangers with and without helically crimped fins. Int Commun Heat Mass Transf. 2007;34(3):321–30. https://doi.org/10.1016/j.icheatmasstransfer.2006.11.009.
2. Zachár A. Analysis of coiled-tube heat exchangers to improve heat transfer rate with spirally corrugated wall. Int J Heat Mass Transf. 2010;53(19–20):3928–39. https://doi.org/10.1016/j.ijheatmasstransfer.2010.05.011.
3. Zhao Z, Wang X, Che D, Cao Z. Numerical studies on flow and heat transfer in membrane helical-coil heat exchanger and membrane serpentine-tube heat exchanger. Int Commun Heat Mass Transf. 2011;38(9):1189–94. https://doi.org/10.1016/j.icheatmasstransfer.2011.06.014.
4. Zachár A. Investigation of natural convection induced outer side heat transfer rate of coiled-tube heat exchangers. Int J Heat Mass Transf. 2012;55(25–26):7892–901. https://doi.org/10.1016/j.ijheatmasstransfer.2012.08.014.
5. Genić SB, Jaćimović BM, Jarić MS, Budimir NJ. Analysis of fouling factor in district heating heat exchangers with parallel helical tube coils. Int J Heat Mass Transf. 2013;57(1):9–15. https://doi.org/10.1016/j.ijheatmasstransfer.2012.09.060.
6. Shi Z, Dong T. Thermodynamic investigation and optimization of laminar forced convection in a rotating helical tube heat exchanger. Energy Convers Manag. 2014;86:399–409. https://doi.org/10.1016/j.enconman.2014.04.055.
7. Mozafari M, Akhavan-Behabadi MA, Qobadi-Arfaee H, Fakoor-Pakdaman M. Condensation and pressure drop characteristics of R600a in a helical tube-in-tube heat exchanger at different inclination angles. Appl Therm Eng. 2015;90:571–8. https://doi.org/10.1016/j.applthermaleng.2015.07.044.
8. Sadighi Dizaji H, Khalilarya S, Jafarmadar S, Hashemian M, Khezri M. A comprehensive second law analysis for tube-in-tube helically coiled heat exchangers. Exp Therm Fluid Sci. 2016;76:118–25. https://doi.org/10.1016/j.expthermflusci.2016.03.012.
9. Sheikholeslami M, Ganji DD. Heat transfer enhancement in an air to water heat exchanger with discontinuous helical turbulators; experimental and numerical studies. Energy. 2016;116:341–52. https://doi.org/10.1016/j.energy.2016.09.120.
10. Zhang C, Wang D, Xiang S, Han Y, Peng X. Numerical investigation of heat transfer and pressure drop in helically coiled tube with spherical corrugation. Int J Heat Mass Transf. 2017;113:332–41. https://doi.org/10.1016/j.ijheatmasstransfer.2017.05.108.
11. Omidi M, Farhadi M, Jafari M. Numerical study on the effect of using spiral tube with lobed cross section in double-pipe heat exchangers. J Therm Anal Calorim. 2018;134(3):2397–408. https://doi.org/10.1007/s10973-018-7579-y.
12. Zhou C, Ni L, Yao Y. Heat transfer analysis of multi-row helically coiled tube heat exchangers for surface water-source heat pump. Energy. 2018;163:1032–49. https://doi.org/10.1016/j.energy.2018.08.190.
13. Mirgolbabaei H. Numerical investigation of vertical helically coiled tube heat exchangers thermal performance. Appl Therm Eng. 2018;136:252–9. https://doi.org/10.1016/j.applthermaleng.2018.02.061.
14. Javadi H, Mousavi Ajarostaghi SS, Pourfallah M, Zaboli M. Performance analysis of helical ground heat exchangers with different configurations. Appl Therm Eng. 2019;154:24–36. https://doi.org/10.1016/j.applthermaleng.2019.03.021.
15. Awais M, Saad M, Ayaz H, Ehsan MM, Bhuiyan AA. Computational assessment of Nano-particulate (Al$_2$O$_3$/Water) utilization for enhancement of heat transfer with varying straight

section lengths in a serpentine tube heat exchanger. Therm Sci Eng Prog. 2020;20:100521. https://doi.org/10.1016/j.tsep.2020.100521.

16. Heydari O, Miansari M, Arasteh H, Toghraie D. Optimizing the hydrothermal performance of helically corrugated coiled tube heat exchangers using Taguchi's empirical method: energy and exergy analysis. J Therm Anal Calorim. 2021;145(5):2741–52. https://doi.org/10.1007/s10973-020-09808-3.

17. Ali SK, Azzawi IDJ, Khadom AA. Experimental validation and numerical investigation for optimization and evaluation of heat transfer enhancement in double coil heat exchanger. Therm Sci Eng Prog. 2021;22:100862. https://doi.org/10.1016/j.tsep.2021.100862.

18. Kumar EP, Solanki AK, Kumar MMJ. Numerical investigation of heat transfer and pressure drop characteristics in the micro-fin helically coiled tubes. Appl Therm Eng. 2021;182:116093. https://doi.org/10.1016/j.applthermaleng.2020.116093.

19. Miansari M, Jafarzadeh A, Arasteh H, Toghraie D. Thermal performance of a helical shell and tube heat exchanger without fin, with circular fins, and with V-shaped circular fins applying on the coil. J Therm Anal Calorim. 2021;143(6):4273–85. https://doi.org/10.1007/s10973-020-09395-3.

20. Fawaz A, Hua Y, Le Corre S, Fan Y, Luo L. Topology optimization of heat exchangers: a review. Energy. 2022;252:124053. https://doi.org/10.1016/j.energy.2022.124053.

21. Aldor A, Moguen Y, El Omari K, Habchi C, Cocquet P-H, Le Guer Y. Heat transfer enhancement by chaotic advection in a novel sine-helical channel geometry. Int J Heat Mass Transf. 2022;193:122870. https://doi.org/10.1016/j.ijheatmasstransfer.2022.122870.

22. Wang G, Liu A, Dbouk T, Wang D, Peng X, Ali A. Optimal shape design and performance investigation of helically coiled tube heat exchanger applying MO-SHERPA. Int J Heat Mass Transf. 2022;184:122256. https://doi.org/10.1016/j.ijheatmasstransfer.2021.122256.

23. Lei Z, Bao Z. Experimental investigation on laminar heat transfer performances of RP-3 at supercritical pressure in the helical coiled tube. Int J Heat Mass Transf. 2022;185:122326. https://doi.org/10.1016/j.ijheatmasstransfer.2021.122326.

24. Marzouk SA, Abou Al-Sood MM, El-Fakharany MK, El-Said EMS. Thermo-hydraulic study in a shell and tube heat exchanger using rod inserts consisting of wire-nails with air injection: experimental study. Int J Therm Sci. 2021;161:106742. https://doi.org/10.1016/j.ijthermalsci.2020.106742.

25. Wang G, Gu Y, Zhao L, Xuan J, Zeng G, Tang Z, et al. Experimental and numerical investigation of fractal-tree-like heat exchanger manufactured by 3D printing. Chem Eng Sci. 2019;195:250–61. https://doi.org/10.1016/j.ces.2018.07.021.

26. Marzouk SA, Abou Al-Sood MM, El-Said EMS, Younes MM, El-Fakharany MK. Experimental and numerical investigation of a novel fractal tube configuration in helically tube heat exchanger. Int J Therm Sci. 2023;187:108175. https://doi.org/10.1016/j.ijthermalsci.2023.108175.

27. Marzouk SA, Abou Al-Sood MM, El-Said EMS, El-Fakharany MK. Effect of wired nails circular–rod inserts on tube side performance of shell and tube heat exchanger: experimental study. Appl Therm Eng. 2020;167:114696. https://doi.org/10.1016/j.applthermaleng.2019.114696.

28. Holman JP, Gajda WJ. Experimental Methods for Engineers, McGraw-Hill, 3rd Ed., 1978.

29. Biçer N, Engin T, Yaşar H, Büyükkaya E, Aydın A, Topuz A. Design optimization of a shell-and-tube heat exchanger with novel three-zonal baffle by using CFD and Taguchi method. Int J Therm Sci. 2020;155:106417. https://doi.org/10.1016/j.ijthermalsci.2020.106417.

30. Aly WIA. Numerical study on turbulent heat transfer and pressure drop of nanofluid in coiled tube-in-tube heat exchangers. Energy Convers Manag. 2014;79:304–16. https://doi.org/10.1016/j.enconman.2013.12.031.

31. He L, Li P. Numerical investigation on double tube-pass shell-and-tube heat exchangers with different baffle configurations. Appl Therm Eng. 2018;143:561–9. https://doi.org/10.1016/j.applthermaleng.2018.07.098.

32. Naqvi SMA, Elfeky KE, Cao Y, Wang Q. Numerical analysis on performances of shell side in segmental baffles, helical baffles and novel clamping anti-vibration baffles with square twisted tubes shell and tube heat exchangers. Energy Procedia. 2019;158:5770–5. https://doi.org/10.1016/j.egypro.2019.01.553.

33. Marzouk SA, Al-Sood MMA, El-Fakharany MK, El-Said EMS. A comparative numerical study of shell and multi-tube heat exchanger performance with different baffles configurations. Int J Therm Sci. 2022;179:107655. https://doi.org/10.1016/j.ijthermalsci.2022.107655.

34. Marzouk SA, El-Fakharany MK, Baz FB. Heat transfer performance of particle solar receiver: Numerical study. Heat Transf Res. 2022;53(13):1–19.

35. Lei Y, Li Y, Jing S, Song C, Lyu Y, Wang F. Design and performance analysis of the novel shell-and-tube heat exchangers with louver baffles. Appl Therm Eng. 2017;125:870–9. https://doi.org/10.1016/j.applthermaleng.2017.07.081.

36. Yunus AC. Fluid mechanics: fundamentals and applications (Si Units). Noida: Tata McGraw Hill Education Private Limited; 2010.